Pressure-Induced Structural Transition and Enhanced Photoelectric Properties of Tm_2S_3

Zhi-Wei Shen(申志伟)[1,2], Zhong-Yan Wu(邬中炎)[2*], Shao-Jie Wang(王绍杰)[1,2], He-Chong Wang(王贺冲)[1,2], Hong-Kai Li(李宏凯)[1,2], Jing Song(宋静)[1,2], Guo-Ying Gao(高国英)[2], Lin Wang(王霖)[2*], and Yong-Jun Tian(田永君)[2]

[1]*Key Laboratory for Microstructural Material Physics of Hebei Province, School of Science, Yanshan University, Qinhuangdao 066004, China*

[2]*Center for High Pressure Science (CHiPS), State Key Laboratory of Metastable Materials Science and Technology (MMST), Yanshan University, Qinhuangdao 066004, China*

(Received 5 September 2024; accepted manuscript online 23 September 2024)

Rare earth sesquisulfides have drawn growing attention in photoelectric applications because of their excellent electronic and photoelectric properties upon compression. We investigate the structural, electrical, and photoelectric properties of Tm_2S_3 under high pressure through electrical impedance, UV-vis absorption, Raman spectroscopy, x-ray diffraction, and photoelectric measurements. It is found that δ-Tm_2S_3 transforms into high-pressure α-phase around 5 GPa, accompanied by a substantial reduction in atomic distance, bandgap, and resistivity. Consequently, the photocurrent density and responsivity of Tm_2S_3 exhibit dramatic increase behavior, achieving five orders of magnitude enhancement in α-phase compared with the initial δ-Tm_2S_3. Moreover, α-phase maintains a high photocurrent responsivity of three orders of magnitude after unloading. This work demonstrates significant enhancement of the photoelectric properties of Tm_2S_3 by applying pressure, which paves the way for improving the performance of future photoelectric devices.

DOI: 10.1088/0256-307X/41/11/117101

Photodetectors are crucial to contemporary technologies, especially in roles central to energy conversion,[1] data processing,[2] and communications.[3] Over the past decades, the quest for higher photoelectric efficiency has stimulated extensive studies about materials with distinct optical and electronic features, such as low-dimensional compounds,[4–9] carbides and nitrides (Mxenes),[10,11] graphene,[12–14] and perovskite materials.[15–17]

Recently, rare earth sesquisulfides (RE_2S_3, RE = La, Pr, Tm, etc.) with unique $4f$ electronic characteristics and excellent semiconductor properties have garnered considerable attention in the domain of photoelectric applications.[18–21] They exhibit excellent photosensitivity and electrical transport properties due to the abundance of electronic states provided by inner-shell electron participation, resulting in unique spectral features during light absorption and emission. In photoelectric conversion and photodetection, these materials offer adjustable bandgap widths and enhanced light absorption, positioning them as potential superior for applications in high-efficiency solar cells and wavelength-selective photodetectors.[18] Furthermore, some rare earth sesquisulfides such as Dy_2S_3, Nd_2S_3, and Gd_2S_3 display commendable thermal stability and chemical corrosion resistance,[22,23] which is vital for stable long-term operation in harsh conditions for photoelectric devices. Rare earth sesquisulfides stand out in photoelectric materials for their superior photoresponse and electrochemical stability, offering considerable promise for creating advanced photoelectric devices. Despite these great potentials, the industrial application of rare earth sesquisulfides in photodetectors is limited due to their high resistivity and large bandgap under ambient conditions. Therefore, novel approaches are demanded to overcome these disadvantages and to further improve the photoelectric performance of rare earth sesquisulfides.

Pressure, as a precise and controllable tool, can modify the physical and photoelectric properties of materials by changing interatomic distances, electronic structures, and crystal lattices.[24–28] For instance, Y_2O_3 crystal transforms into amorphous due to pressure-driven lattice distortions.[29] Similar pressure-induced structural changes have been observed in Lu_2S_3 and Ho_2S_3.[30,31] In our previous study, we demonstrated that pressure can induce a noticeable leap in photocurrent near the structural phase transition in Y_2S_3.[21] Having the same δ crystal structure and similar physical properties as Y_2S_3, Tm_2S_3 is expected to exhibit outstanding photoelectric properties under high pressure and has important implications for rare earth sesquisulfides photodetectors. However, no relevant experimental results are reported in the literature and little is known about the high-pressure photoelectric effect of Tm_2S_3.

In this study, we focus on altering the photoelectric properties of Tm_2S_3 by applying pressure. The results of

*Corresponding authors. Email: wuzhongyan@ysu.edu.cn; linwang@ysu.edu.cn

© 2024 Chinese Physical Society and IOP Publishing Ltd

photocurrent measurement under high pressure indicate a significant enhancement in the photoresponse of Tm_2S_3. Under compression, the response spectrum extends into the near-infrared range. Additionally, the photocurrent of Tm_2S_3 maintains three orders of magnitude higher than the initial value after pressure release. *In situ* x-ray diffraction (XRD), Raman spectroscopy, electrical transport, and UV-vis analysis suggest that the phase transition of Tm_2S_3 leads to significant changes in its physical properties, which accounts for its appealing high-pressure photoelectric characteristics.

Experiments. The photocurrents of Tm_2S_3 powder (99.9%, Beijing Hawk Science & Technology) were recorded in a symmetric diamond anvil cell (DAC) with a culet size of 300 μm through a two-probe resistance method up to a maximum pressure of about 18 GPa. To ensure no contact between electrodes and T301 steel gaskets, a mixture of epoxy and cubic boron nitride was used as an insulating layer on the gaskets. Under bias voltages, time-dependent photocurrents under 360 nm laser irradiation were recorded using a Keithley 2461 SourceMeter. *In situ* high-pressure impedance measurements were carried out with a Solartron 1260&1296 impedance analyzer up to 42 GPa. High-pressure electrical transport measurements were carried out by employing the van der Pauw method with four Pt foil without any pressure medium in a commercial DynaCool physical property measurement system (PPMS, Quantum Design).[32] The ruby fluorescence method was used to determine pressure.[33] High-pressure XRD experiments were performed using Rigaku XtaLAB Synergy Custom, with an x-ray wavelength of 0.5594 Å. Structural refinements were performed using the Rietveld method in the GSAS software.[34] In Raman and UV-vis absorption measurements, neon was used as the pressure transmitting medium. The high-pressure Raman spectra were measured in a high-resolution confocal micro-Raman spectrometer (HR Evolution, JY Horiba, Japan) with 633 nm laser excitation source. The UV-vis absorption spectra were recorded with an Oceanoptics DH-2000-BAL deuterium-halogen light source.

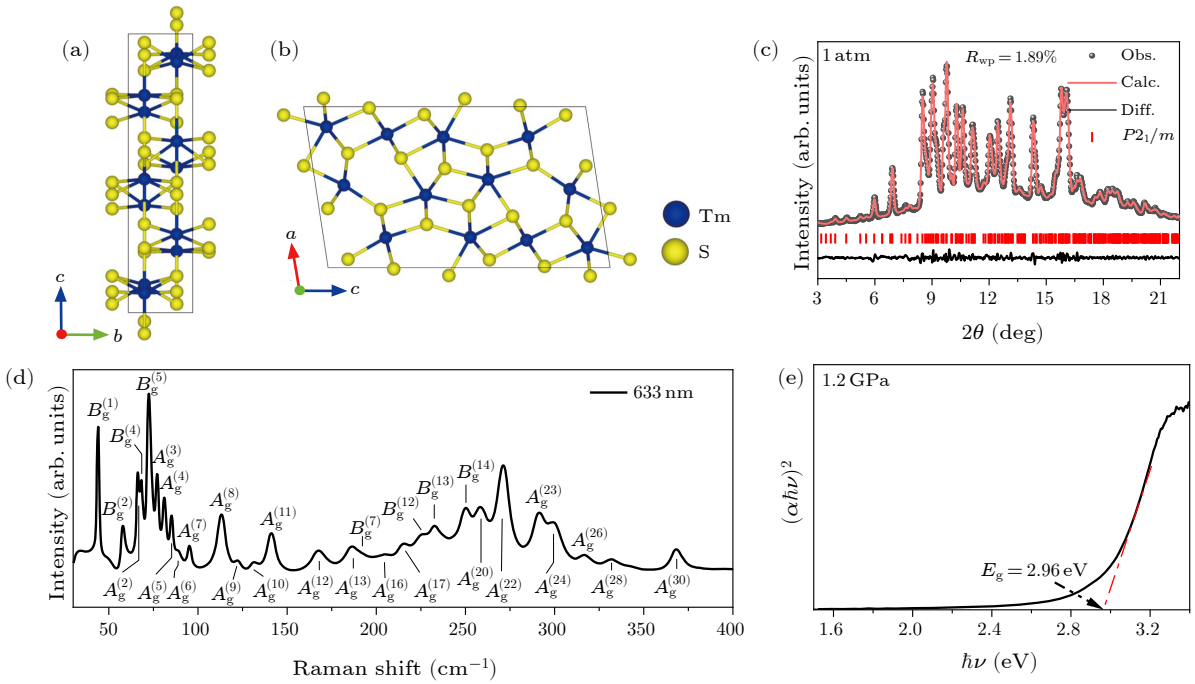

Fig. 1. Crystal structure of Tm_2S_3 viewed along (a) [100] direction and (b) [010] direction. (c) XRD pattern of Tm_2S_3 with space group $P2_1/m$ at 1 atm. (d) Raman spectra of Tm_2S_3 with Raman modes under ambient conditions. (e) Tauc plot of Tm_2S_3 with a bandgap of 2.96 eV under 1.2 GPa.

Results and Discussions. The fundamental physical properties of Tm_2S_3 are characterized through XRD, Raman, and UV-vis absorption spectroscopy, in agreement with the results from previous studies.[35–37] XRD result reveals that Tm_2S_3 adopts a monoclinic structure within $P2_1/m$ space group (δ-phase),[36] where the thulium (Tm) and sulfur (S) atoms arrange into regular octahedral coordination as shown in the schematic drawings in Figs. 1(a) and 1(b). Half of the Tm atoms are six-fold coordinated and the others are seven-fold coordinated.[38] A Rietveld refinement profile is shown in Fig. 1(c) and the lattice parameters are determined as $a = 10.0787$ Å, $b = 3.9761$ Å, $c = 17.4721$ Å, $\beta = 98.66°$, and $V_0 = 692.189$ Å^3. Raman spectrum in Fig. 1(d) shows abundant peaks below 400 cm^{-1}, but the overlapped features and attenuation of the Raman peaks obscure the full representation of 45 Raman-active modes ($30A_g + 15B_g$) in the factor group calculation.[36] The optical bandgap of Tm_2S_3 is characterized by UV-vis absorption spectroscopy. Using the Tauc plot method in Fig. 1(e), the bandgap of Tm_2S_3, a

direct-gap semiconductor,[39] is estimated to be 2.96 eV at 1.2 GPa.

As illustrated in Figs. 2(a) and 2(b), a photoelectric device in a DAC is coupled with 360 nm laser illumination and external electrodes to evaluate the photoresponse of Tm_2S_3 under high pressure. At a steady pressure of 0.8 GPa [Fig. 2(c)], the experiments were conducted in a series of repeated on/off cycles (30 s) with various incident light power densities (P_{in}) at several bias voltages (V). To quantitatively describe the photoelectric behavior with changes in V and P_{in}, two pivotal parameters are identified for the photodetector: the photocurrent density J_{ph} and the responsivity R:

$$J_{ph} = \frac{I_{ph}}{S}, \tag{1}$$

$$R = \frac{I_{ph}}{P_{in} \cdot S}, \tag{2}$$

where photocurrent (I_{ph}) is defined as $I_{ph} = I_{illumination} - I_{dark}$, and S represents the effective illuminated area. As demonstrated in Figs. 2(d)–2(e), J_{ph} linearly increases from 11.42 to 21.28 $nA \cdot mm^{-2}$ as P_{in} increases from 12 to 20 $mW \cdot mm^{-2}$. This notably proportional relationship indicates the effective separation and conveyance of photogenerated carriers, suggesting the excellent light absorption characteristics of Tm_2S_3. The I–V characteristics under different P_{in} in Fig. S1 of the Supporting Information reveal that the photocurrent increases with bias voltages without saturation below 5 V.

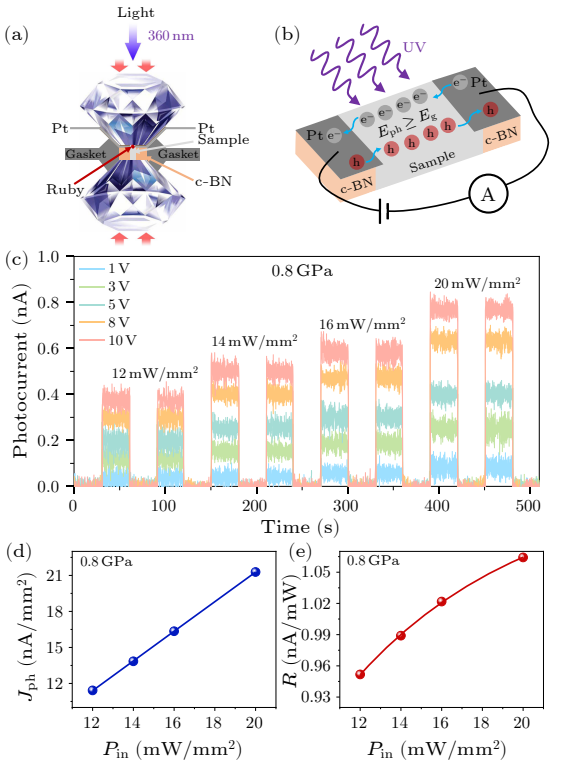

Fig. 2. (a) Schematic of the photoelectric device in a DAC setup. (b) Schematic of *in situ* photoelectric effect. (c) Photocurrent of Tm_2S_3 under an applied pressure of 0.8 GPa, exhibiting variations with different voltages and incident light power intensities (12–20 $mW \cdot mm^{-2}$). Variation of photocurrent density J_{ph} (d) and responsivity R (e) with incident laser intensity at a 5 V bias.

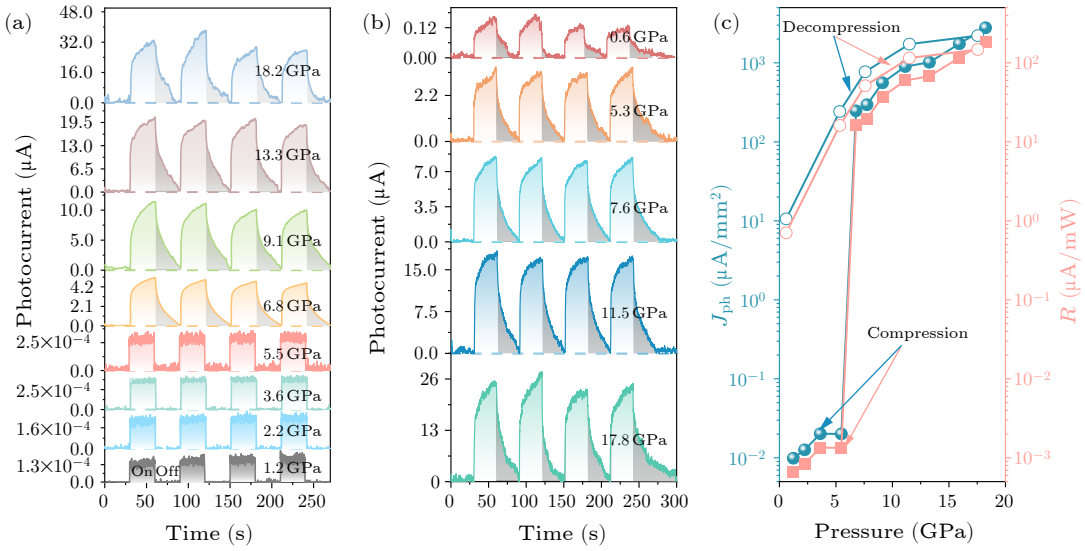

Fig. 3. Photocurrent response of Tm_2S_3 under illumination from a 360 nm laser at bias of 5 V: (a) during compression and (b) during decompression. (c) Extracted pressure-dependent photocurrent density (J_{ph}) and responsivity (R) from compression and decompression cycles.

To evaluate the pressure effect on the photoresponse of Tm_2S_3, *in situ* photoelectric measurements were performed up to 18.2 GPa with a fixed bias voltage of 5 V. P_{in} is fixed at 15 $mW \cdot mm^{-2}$ to avoid the thermal effect during measurements. The fluctuations in the photocurrent during compression and decompression are illustrated in Figs. 3(a) and 3(b), respectively. The sudden surge in photocurrent observed upon illumination is primarily ascribed to the rapid generation of charge carriers.[40,41] This phenomenon is fundamentally tied to the internal photo-

electric effect in semiconductor materials, where the electrons are excited from valence band to the conduction band immediately after absorbing the photon energy. As seen from the height of the square-shaped peaks in Fig. 3(a), the photocurrent increases slowly with the elevated pressure below 5.5 GPa. However, as the pressure increases to 6.8 GPa, the photocurrent suddenly increases four orders of magnitude. Meanwhile, the photocurrent peaks show slopes upon laser on/off, indicating the decline of the photoresponse rate. The sluggish photoresponse is mainly attributed to the photothermal effect,[42,43] where the trap state can be neglected because of the low trap density in Tm_2S_3.[44]

The pressure-dependent J_{ph} and R follow the same trends during compression and decompression as shown in Fig. 3(c). At the initial pressure of 1.2 GPa, R and J_{ph} are relatively small, with a value of 6.58×10^{-4} μA·mW^{-1} and 9.8×10^{-3} μA·mm^{-2}, respectively. These values become doubled at 5.5 GPa and experience a dramatic increase above this threshold pressure, achieving a striking value of 16.5 μA·mW^{-1} for R and 246.9 μA·mm^{-2} for J_{ph} at 6.8 GPa. With pressure further increasing to 18.2 GPa, R and J_{ph} continuously increase to 185.3 μA·mW^{-1} and 2.8×10^3 μA·mm^{-2}, respectively. As a result, the application of high-pressure successfully induces an incredible enhancement in the photoelectric properties of Tm_2S_3 with five orders of magnitude increase from 1.2 GPa to 18.2 GPa. For comparison, the magnitudes of the pressure-enhanced photoelectric properties are only three and two orders in $ZnGeP_2$[42] and WS_2,[43] respectively. After releasing the pressure to 0.6 GPa, R and J_{ph} of Tm_2S_3 remain three orders of magnitude higher than the initial values at 1.2 GPa. The maintained high photocurrent density and responsivity highlight the promising industrial applications for the pressure-enhanced photoelectric effect in Tm_2S_3.

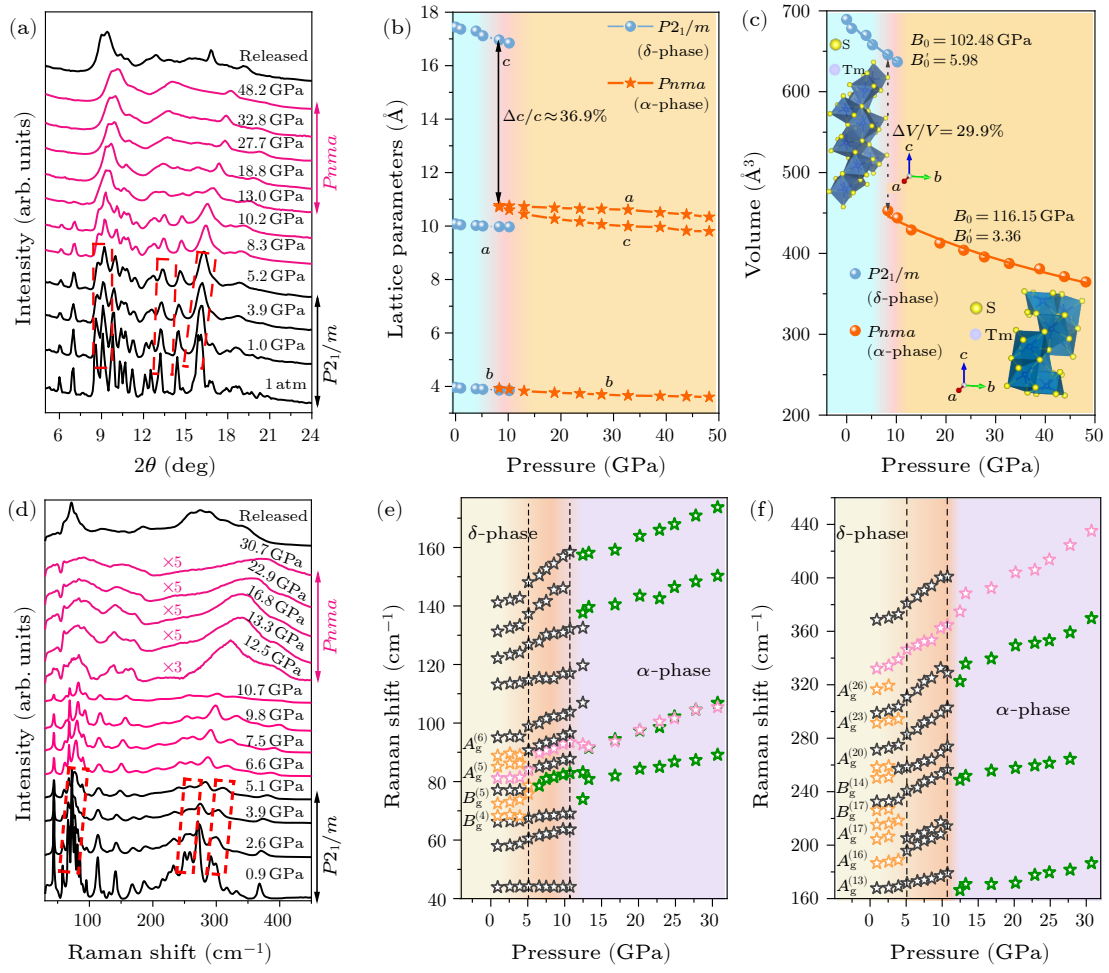

Fig. 4. (a) XRD patterns for Tm_2S_3 under high pressures. (b) Lattice parameters evolution of Tm_2S_3 under different pressures. (c) Pressure-volume curve of Tm_2S_3 during compression. (d) Raman spectra of Tm_2S_3 under high pressures. (e)–(f) Pressure dependence of the Raman shifts under compression.

To further understand the mechanism of the pressure-enhanced photoelectric properties of Tm_2S_3, *in situ* XRD and Raman measurements were performed to investigate the modulation of the crystal structures and molecular vibrations under high pressure. Indeed, a phase transition is found around 5 GPa, in coincidence with the pressure of the photoelectric effect boost. As depicted in Figs. 4(a) and 4(d), the application of pressure results in the disap-

pearance of several XRD peaks (9.05, 9.67, 9.87, 13.17, 14.67 and 15.7°) and the merging of Raman peaks above 5.2 GPa, indicating the initiation of a phase transition. The phase transition zone covers a broad pressure range and is eventually completed with a single high-pressure phase above 10 GPa. At 12.5 GPa, twelve Raman peaks [marked in orange and labeled in Figs. 4(e) and 4(f)] disappear, while new peaks (marked in green) appear at 73.99, 78.58, 137.72, 157.52, 166.34, 248.82, and 322.6 cm^{-1}, as shown in Figs. 4(e) and 4(f). Upon further compression, most Raman peaks become indiscernible and lost in the background due to overlapping.

Comparative analysis with previous reports[21,45] suggests an orthorhombic structure ($Pnma$) for the high-pressure α-phase of Tm_2S_3, as illustrated in Figs. S3(a), S3(b), and S3(d). The lattice parameters are $a = 10.77$ Å, $b = 3.92$ Å and $c = 10.71$ Å at 8.2 GPa. This high-pressure phase remains stable up to 48.2 GPa without further transitions. As shown in Fig. 4(c), the bulk modulus (B) for δ- and α-phases are determined by fitting the pressure–volume (P–V) data with a third-order Birch–Murnaghan equation of state:[46]

$$P(V) = \frac{3B_0}{2}\left[\left(\frac{V_0}{V}\right)^{\frac{7}{3}} - \left(\frac{V_0}{V}\right)^{\frac{5}{3}}\right] \cdot \left\{1 + \frac{3}{4}(B' - 4)\left[\left(\frac{V_0}{V}\right)^{\frac{2}{3}} - 1\right]\right\}, \quad (3)$$

yielding values of 102.48 GPa and 116.15 GPa, respectively. The smaller bulk modulus of the δ-phase indicates that it is more compressible than the α-phase. Nearby the phase boundary as depicted in Figs. 4(b) and 4(c), lattice parameter c has a large collapse with a decrease of about 36.9%, and the lattice volume shows a discontinuity with a noticeable reduction of 29.9%. The phase transition is irreversible as evidenced by the retained high-pressure XRD [see Fig. S3(c) in the Supporting Information] and Raman patterns after releasing to ambient.

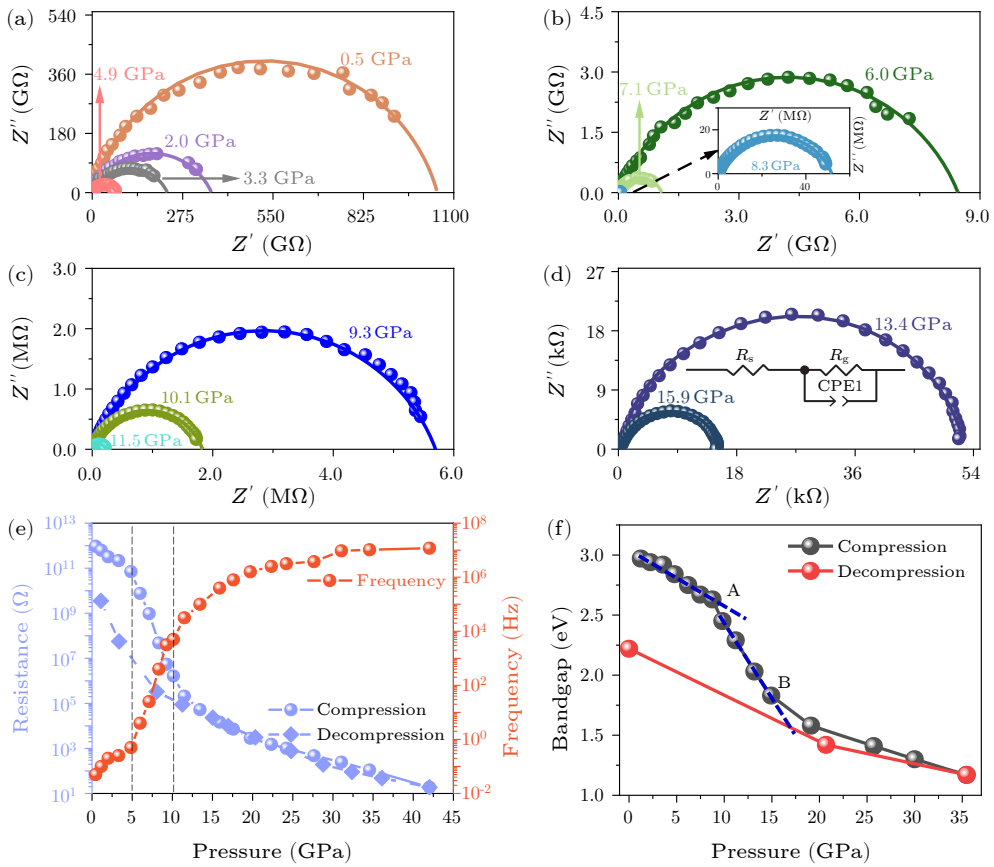

Fig. 5. The Nyquist plots for Tm_2S_3 obtained from impedance spectroscopy at selected pressures: (a) 0.5–4.9 GPa, (b) 6.0–8.3 GPa, (c) 9.3–11.5 GPa, (d) 13.4–15.9 GPa. The solid line indicates the fitting result, and the solid symbols represent the actual experimental data. The equivalent circuit model used to fit these plots is depicted in (d). (e) Pressure dependence of resistance (left axis) and relaxation frequency (right axis). (f) The bandgap variation of Tm_2S_3 as a function of pressure.

The dramatic changes in atomic distance and interactions brought by structural transition can alter the electrical characteristics of Tm_2S_3, which are crucial factors influencing the photoelectric properties. In order to recognize the relationship between photoelectric and electrical properties, we performed AC impedance spectroscopy experiments. The Nyquist plots of impedance spectra of Tm_2S_3 at selected pressures are shown in Figs. 5(a)–5(d).

As seen from the single semicircle in the impedance spectra, the contribution of grain boundary and grain are overlapped and not easily distinguishable in the Nyquist plot. The diameter of the semicircles becomes smaller with increasing pressure, suggesting a reduction in resistance.

To quantify the electrical resistances and relaxation frequency of Tm_2S_3, all of these measured Nyquist and Bode plots are fitted using an equivalent circuit model [see Fig. 5(d)] in the Zview software. As shown in Fig. 5(e), the resistance of Tm_2S_3 decreases slowly with pressure increasing from 0.5 GPa to 4.9 GPa, and then decreases rapidly above 4.9 GPa. At 10.1 GPa, the resistance of Tm_2S_3 drops seven orders of magnitude from its initial value, while the frequency shifts from low to high, indicating a significant increase in carrier concentration during compression.[47] The dramatic change in resistance and relaxation frequency with pressure is an important reason for the enhanced photocurrent around 5 GPa.

Bandgap plays an important role in the photoelectric process for semiconductor materials, which is directly related with the ability of absorbing photons and generating photocarriers.[40] To investigate the bandgap evolution of Tm_2S_3 under high pressures, we conducted *in situ* UV-vis absorption spectroscopy experiments up to 35.5 GPa, as illustrated in Fig. S4. Using the Tauc plot method, we establish the relationship between the bandgap and pressure for Tm_2S_3 from 1.2 GPa to 35.5 GPa. As illustrated in Fig. 5(f), the bandgap of Tm_2S_3 decreases upon compression with a distinct kink to a faster decline around 10 GPa, where the structure completely transforms to α-phase. The linearly fitted decreasing rates of bandgap below and above 10 GPa are 0.045 eV/GPa (line A) and 0.121 eV/GPa (line B), respectively. The narrowing of bandgap under pressure facilitates the excitation of valence electrons by light, leading to an increase in photogenerated carriers and, consequently, higher photocurrent density.[43]

The pressure evolution of resistance and bandgap are in line with the phase transition. As increasing pressure across the δ–α-phase transition, the reduced atomic distance experiences a substantial drop along the c-axis, which greatly enhances the interactions among atoms and facilitates the charge transfer. As a result, the bandgap narrows and the conductivity becomes higher, contributing to the significantly enhanced photoelectric properties. After unloading, the retained α-phase demonstrates a relatively low resistance (three orders of magnitude smaller) and narrowed bandgap (25.3% smaller) compared with the initial values of the δ-phase, thus keeping the high photocurrent density and responsivity. Compared with the δ-phase at ambient (Table S1 in the Supporting Information), the lattice volume of the decompressed α-Tm_2S_3 sample is considerably smaller, further confirming the maintained high-pressure structural, electrical, and photoelectric properties.

In conclusion, this study has successfully demonstrated significant pressure-enhanced photocurrent density and responsivity of Tm_2S_3, with five orders of magnitude increase from 1.2 GPa to 18.2 GPa. Upon compression, XRD and Raman measurements reveal a pressure-induced structural transition from the monoclinic $P2_1/m$ δ-phase to the orthorhombic $Pnma$ α-phase around 5 GPa. The observed enhancements in photoelectric properties are attributed to the substantially reduced atomic distance, bandgap, and impedance across the δ–α-phase transition, which facilitates the charge transfer and thus increases photogenerated carriers. The stability of the retained α-phase after unloading suggests that the pressure-enhanced photoelectric properties of Tm_2S_3 are persistent and robust.

Overall, our findings highlight high pressure as a feasible strategy for enhancing the photoelectric properties of rare earth sesquisulfides. The maintained high photocurrent responsivity from the retained high-pressure phase after unloading posits Tm_2S_3 as a promising candidate for future photoelectric applications.

Acknowledgement. This work was mainly supported by the National Natural Science Foundation of China (Grant Nos. 52288102, 52090020, 52022089, and 52372261).

References

[1] Xiao K, Chen L, Chen R, Heil T, Lemus S D C, Fan F, Wen L, Jiang L, and Antonietti M 2019 *Nat. Commun.* **10** 74
[2] Kwak D, Polyushkin D K, and Mueller T 2023 *Nat. Commun.* **14** 4264
[3] Li Z, Li Q, Li H, Yue L, Zhao D, Tian F, Dong Q, Zhang X, Jin X, Zhang L, Liu R, and Liu B 2022 *Adv. Funct. Mater.* **32** 2108636
[4] Wu X, Zhang H B, Zhang J, and Lou X W 2021 *Adv. Mater.* **33** 2008376
[5] Duan X, Wang C, Pan A, Yu R, and Duan X 2015 *Chem. Soc. Rev.* **44** 8859
[6] Gong C, Zhang Y, Chen W *et al.* 2017 *Adv. Sci.* **4** 1700231
[7] Manzeli S, Ovchinnikov D, Pasquier D, Yazyev O V, and Kis A 2017 *Nat. Rev. Mater.* **2** 17033
[8] Guo S, Mihalyi-Koch W, Mao Y *et al.* 2024 *Nat. Commun.* **15** 3001
[9] Luo H, Bu K, Yin Y *et al.* 2023 *Angew. Chem. Int. Ed.* **62** e202304494
[10] Liu T, Zhang C, and Li X 2022 *Adv. Opt. Mater.* **10** 2201153
[11] Xu H, Ren A, Wu J, and Wang Z 2020 *Adv. Funct. Mater.* **30** 2000907
[12] Yoshioka K, Wakamura T, Hashisaka M, Watanabe K, Taniguchi T, and Kumada N 2022 *Nat. Photon.* **16** 718
[13] Zhang B Y, Liu T, Meng B, Li X, Liang G, Hu X, and Wang Q J 2013 *Nat. Commun.* **4** 1811
[14] Koppens F H L, Mueller T, Avouris P, Ferrari A C, Vitiello M S, and Polini M 2014 *Nat. Technol.* **9** 780
[15] Li Y, Shi Z, Liang W, Ma J, Chen X, Wu D, Tian Y, Li X, Shan C, and Fang X 2021 *Mater. Horiz.* **8** 1367
[16] Zhang Y, Ma Y, Wang Y, Zhang X, Zuo C, Shen L, and Ding L 2021 *Adv. Mater.* **33** 2006691
[17] Guo S, Li Y, Mao Y *et al.* 2022 *Sci. Adv.* **8** eadd1984
[18] Gul M M, Ahmad K S, Thomas A G, Almanqur L, Alharbi Y T, and Alderhami S A 2023 *J. Phys. Chem. Solids* **183** 111646
[19] Raj I L P, Valanarasu S, Trabelsi A B G, Alkallas F H, Shkir M, AlFaify S, and Saxena K K 2023 *Mater. Chem. Phys.* **308** 128282
[20] Mauricot R, Bullot J, Wery J, and Evain M 1996 *Mater. Res. Bull.* **31** 263

[21] Shen Z, Wang L, Yue L, Wang S, Yang K, Li Q, Liu Y, Gao G, Wang L, and Tian Y 2023 *Appl. Mater. Today* **35** 102008
[22] Henderson J R, Muramoto M, Loh E, and Gruber J B 1967 *J. Chem. Phys.* **47** 3347
[23] Taher S M A, Gruber J B, and Olsen L C 1974 *J. Chem. Phys.* **60** 2050
[24] Ren X, Yan X, Yu Z, Li W, and Wang L 2017 *J. Alloys Compd.* **725** 941
[25] Ren X, Yan X, Yu Z, Li W, Yang K, Wang X, Liu Y, and Wang L 2018 *Appl. Phys. Lett.* **112** 143102
[26] Baadji N and Sanvito S 2012 *Phys. Rev. Lett.* **108** 217201
[27] Wang Y, Lü X, Yang W, Wen T, Yang L, Ren X, Wang L, Lin Z, and Zhao Y 2015 *J. Am. Chem. Soc.* **137** 11144
[28] Jing X, Zhou D, Sun R, Zhang Y, Li Y, Li X, Li Q, Song H, and Liu B 2021 *Adv. Funct. Mater.* **31** 2100930
[29] Wang L, Yang W G, Ding Y, Ren Y, Xiao S G, Liu B B, Sinogeikin S V, Meng Y, Gosztola D J, Shen G Y, Hemley R J, Mao W L, and Mao H K 2010 *Phys. Rev. Lett.* **105** 095701
[30] Grzechnik A 2000 *J. Alloys Compd.* **299** 137
[31] Yan X, Ren X, He D, Chen B, and Yang W 2014 *J. Appl. Phys.* **116** 033507
[32] van der Pauw L J 1958 *Philips Res. Rep.* **13** 1
[33] Mao H K, Xu J, and Bell P M 1986 *J. Geophys. Res. Solid Earth* **91** 4673
[34] Toby B H and von Dreele R B 2013 *J. Appl. Cryst.* **46** 544
[35] Sleight A W and Prewitt C T 1968 *Inorg. Chem.* **7** 2282
[36] Knight D S and White W B 1990 *Spectrochim. Acta A* **46** 381
[37] Gigineishvili A V, Dzhabua Z U, Davitadze K D, and Glurdzhidze L N 1995 *Thin Solid Films* **261** 248
[38] Kończyk J, Demchenko P, Bodak O *et al.* 2008 *Chem. Met. Alloys* **1** 38
[39] Yuan H, Zhang J, Yu R, and Su Q 2009 *J. Rare Earths* **27** 308
[40] Ye M, Li Y, Tang R *et al.* 2022 *Nanoscale* **14** 2668
[41] Zhang G, Zhang Q, Hu Q, Wang B, and Yang W 2019 *J. Mater. Chem. A* **7** 4019
[42] Fang S, Li Z, Li R, Jing X, Yue L, Liu R, Yao Z, Li Q, and Liu B 2023 *J. Phys. Chem. C* **127** 22850
[43] Zhang X, Dong Q, Li Z, Jing X, Liu R, Liu B, Zhao T, Lin T, Li Q, and Liu B 2022 *Mater. Res. Lett.* **10** 547
[44] Wang N, Zhang G, Wang G, Feng Z, Li Q, Zhang H, Li Y, and Liu C 2024 *Small* **20** 2400216
[45] Range K J and Leeb R 1975 *Naturforsch B* **30** 889
[46] Birch F 1947 *Phys. Rev.* **71** 809
[47] Nayak A P, Yuan Z, Cao B *et al.* 2015 *ACS Nano* **9** 9117